Geophysical Journal International

Geophys. J. Int. (2015) **202,** 1407–1418
GJI Seismology

doi: 10.1093/gji/ggv229

No thermal anomalies in the mantle transition zone beneath an incipient continental rift: evidence from the first receiver function study across the Okavango Rift Zone, Botswana

Y. Yu,[1] K.H. Liu,[1] M. Moidaki,[2] C.A. Reed[1] and S.S. Gao[1]

[1] *Geology and Geophysics Program, Missouri University of Science and Technology, Rolla, MO* 65409*, USA. E-mail: sgao@mst.edu*
[2] *Department of Physics, University of Botswana, Gaborone, Botswana*

Accepted 2015 May 29. Received 2015 May 3; in original form 2014 December 20

SUMMARY

Mechanisms leading to the initiation and early-stage development of continental rifts remain enigmatic, in spite of numerous studies. Among the various rifting models, which were developed mostly based on studies of mature rifts, far-field stresses originating from plate interactions (passive rifting) and nearby active mantle upwelling (active rifting) are commonly used to explain rift dynamics. Situated atop of the hypothesized African Superplume, the incipient Okavango Rift Zone (ORZ) of northern Botswana is ideal to investigate the role of mantle plumes in rift initiation and development, as well as the interaction between the upper and lower mantle. The ORZ developed within the Neoproterozoic Damara belt between the Congo Craton to the northwest and the Kalahari Craton to the southeast. Mantle structure and thermal status beneath the ORZ are poorly known, mostly due to a complete paucity of broad-band seismic stations in the area. As a component of an interdisciplinary project funded by the United States National Science Foundation, a broad-band seismic array was deployed over a 2-yr period between mid-2012 and mid-2014 along a profile 756 km in length. Using *P*-to-*S* receiver functions (RFs) recorded by the stations, the 410 and 660 km discontinuities bordering the mantle transition zone (MTZ) are imaged for the first time. When a standard Earth model is used for the stacking of RFs, the apparent depths of both discontinuities beneath the Kalahari Craton are about 15 km shallower than those beneath the Congo Craton. Using teleseismic *P*- and *S*-wave traveltime residuals obtained by this study and lithospheric thickness estimated by previous studies, we conclude that the apparent shallowing is the result of a 100–150 km difference in the thickness of the lithosphere between the two cratons. Relative to the adjacent tectonically stable areas, no significant anomalies in the depth of the MTZ discontinuities or in teleseismic *P*- and *S*-wave traveltime residuals are found beneath the ORZ. These observations imply an absence of significant thermal anomalies in the MTZ and in the upper mantle beneath the incipient rift, ruling out the role of mantle plumes in the initiation of the ORZ. We propose that the initiation and development of the ORZ were the consequences of relative movements between the South African block and the rest of the African plate along a zone of lithospheric weakness between the Congo and Kalahari cratons. An area of thinner-than-normal MTZ is found at the SW corner of the study area. This anomaly, if confirmed by future studies, could suggest significant transferring of heat from the lower to the upper mantle.

Key words: Wave propagation; Cratons; Continental tectonics: extensional.

1 INTRODUCTION

The mechanisms controlling the initiation and development of continental rifting can be generally categorized into active and passive processes, wherein the principle distinction depends upon the driving forces that promote lithospheric extension (Sengor & Burke 1978). Active rifting is broadly induced by a hot, actively upwelling asthenosphere followed by extensive magmatic diking and regional uplift, while passive rifting demonstrates crustal extension ambiguously accompanied by volcanism or uplift, and is commonly caused by far-field plate driving forces (Sengor & Burke 1978; White & McKenzie 1989; Schmeling 2010). Observations on the state of rifting and the geodynamic controls governing their evolution were primarily obtained, however, from relatively mature rift zones such

as the Main Ethiopian and Kenyan Rifts of the northernmost East African Rift System (EARS). Meanwhile, the characterization of the initiation and early-stage evolution of continental rifting, exemplified by the amagmatic southern and southwestern EARS rift segments such as the Malawi (Ebinger *et al.* 1984) and Okavango rift zones, is largely underdeveloped.

The Okavango Rift Zone (ORZ), located in northern Botswana, is believed to be an incipient rift at the terminus of the southwestern branch of the EARS (Reeves 1972; Modisi *et al.* 2000). The ORZ is mainly situated within the Neoproterozoic Damara belt and the reworked Paleo-Mesoproterozoic crust of the Rehoboth Province, which are sandwiched between the Neoproterozoic Congo Craton to the northwest and the composite Archean Kalahari Craton (which, in the study area, includes the Kaapvaal and Zimbabwe cratons and the Limpopo belt) to the east–southeast (Hanson 2003; Kinabo *et al.* 2008; Begg *et al.* 2009; Fig. 1). The Damara belt is a Pan-African suture formed during east and west Gondwanaland collision, or is a collapsed intracontinental basin (Stern 1994). It is a major zone of lithospheric weakness in southern Africa, extending from Namibia on the southwestern African coast northeastwards into Zambia (Begg *et al.* 2009).

Surface geological observations and crustal geophysical studies indicate that the ORZ is in its earliest recognizable stage of development, with initiation of rifting estimated to be between 40 and 27 ka (Modisi *et al.* 2000; Kinabo *et al.* 2008; Miensopust *et al.* 2011; Bufford *et al.* 2012). High heat flux has been recorded within a 60 km wide NE-trending zone within the ORZ indicative of substantial fluid migration along rift-related fault zones, suggesting pervasive lithospheric-scale faulting despite the immaturity of the rift zone (Leseane *et al.* 2015). Due to a complete paucity of broadband seismic stations in the vicinity of the ORZ, the structure and thermal state of the upper mantle and the mantle transition zone (MTZ) have not been investigated with sufficient spatial resolution beneath the incipient rift.

Numerous previous studies suggest that the MTZ, which is confined by seismic discontinuities at approximate depths of 410 km and 660 km (hereafter referred to as d410 and d660, respectively), is sensitive to variations in mantle composition and temperature in the vicinity of the discontinuities (Helffrich 2000). Mineral physics and seismological investigations (Ringwood 1975) suggest that d410 is associated with the transition from olivine to wadsleyite, and d660 represents the transition from ringwoodite to perovskite. Relatively

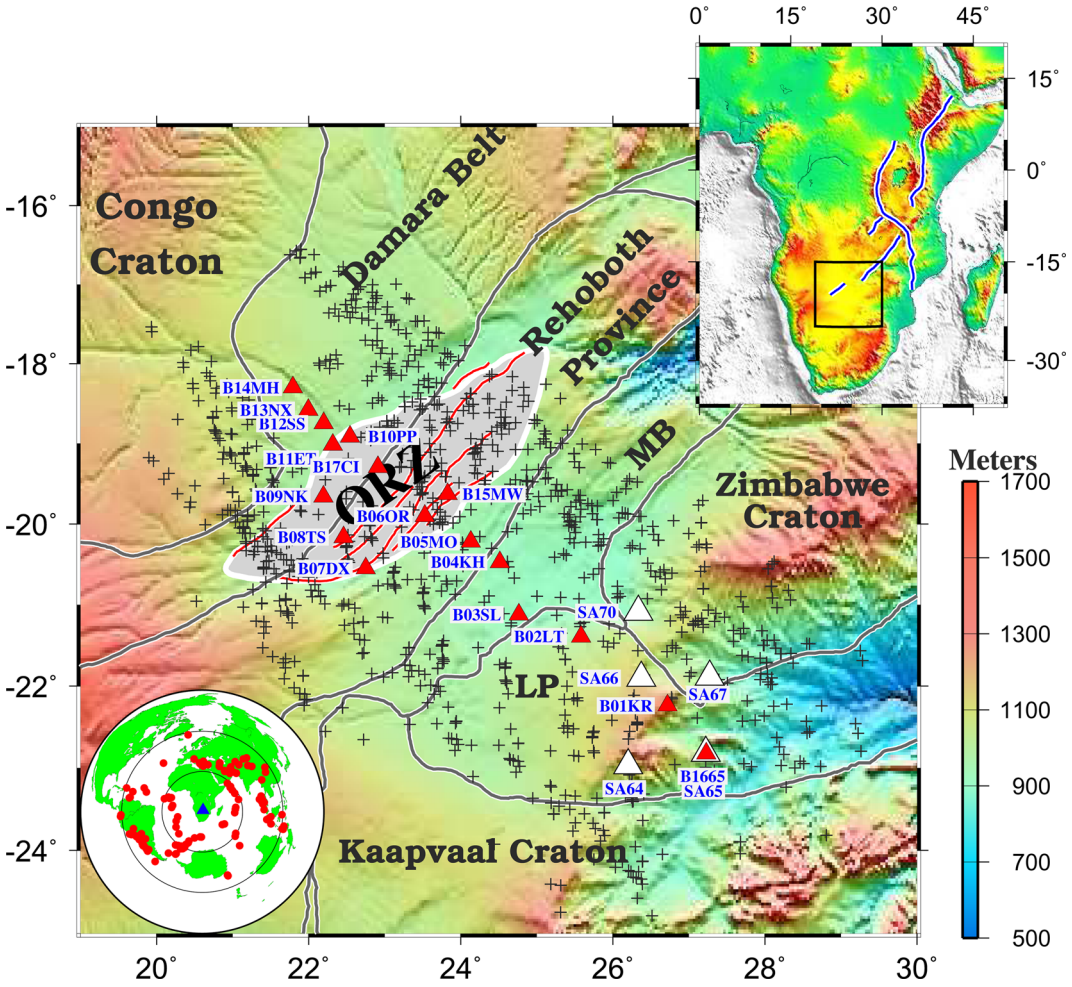

Figure 1. A topographic relief map of the study area showing the SAFARI (red triangles) and SASE (white triangles) seismic stations used in the study. Crosses are ray-piercing points above the depth of 535 km. Red lines show active faults (Kinabo *et al.* 2008) and grey lines delineate boundaries of major tectonic units modified from Hanson (2003) and McCourt *et al.* (2013). LP: Limpopo Belt, MB: Magondi Belt, ORZ: Okavango Rift Zone. The fan-shaped area enclosed by the white lines is the Okavango Delta. The inset in the upper-right corner shows the study area which is indicated by the black rectangle. The blue lines in the inset represent the rift axes of the East African Rift System. The inset in the lower-left corner is an azimuthal equidistant projection map centred at the study area, showing the distribution of earthquakes (red dots) used for the receiver function study.

colder and warmer regions are expected to have thicker and thinner MTZ, respectively, due to their characteristic Clapeyron slopes (about +1.5 to +3.0 MPa K^{-1} for d410 and −4.0 to −0.4 MPa K^{-1} for d660; Ringwood 1975; Bina & Helffrich 1994; Litasov *et al.* 2005; note the significant differences in the values determined by previous studies). Global and regional studies suggest that the observed thick MTZ beneath subduction zones is associated with thermal anomalies ranging between −100 and −300 K, and the deepening d410 beneath hotspots corresponds to thermal anomalies between +100 and +300 K (Tauzin *et al.* 2008). A +200 to +300 K increase in MTZ temperature was proposed to explain the observed depression of d410 beneath the mature sections of the EARS (Nyblade *et al.* 2000; Owens *et al.* 2000; Huerta *et al.* 2009; Mulibo & Nyblade 2013). The presence of water in the MTZ can have the same effect as decreasing temperature and will subsequently thicken the MTZ (Litasov *et al.* 2005). The existence of water has been proposed to explain the observed thicker-than-normal MTZ beneath southern Africa (Blum & Shen 2004), the Nubian and Arabian plates adjacent to the Red Sea (Mohamed *et al.* 2014), and the Afar Depression (Thompson *et al.* 2015). Hence, variations in MTZ thickness and depths of the MTZ discontinuities can behave as a proxy with which to detect the existence of thermal and compositional anomalies and help distinguish the mode of rifting.

Such a tool has been applied to other regions of continental rifting. For instance, the Baikal rift was found to have a cold MTZ based on an observed uplifted d410 (Liu & Gao 2006), and studies in the Rio Grande rift suggested the lack of a large-scale thermal anomaly in the MTZ (Wilson *et al.* 2005; Gao & Liu 2014a). Beneath the Kenya and Tanzania segments of the EARS, receiver function (RF) studies revealed a thin MTZ, which was interpreted to be associated with the African Superplume (Huerta *et al.* 2009; Mulibo & Nyblade 2013). In contrast, beneath southern Africa, Gao *et al.* (2002) observed a normal MTZ thickness and concluded that the African Superplume, if it exists, is constrained in the lower mantle beneath the study area. This conclusion is supported by the seismic tomography study of James *et al.* (2001). The present study represents the first seismological investigations of the upper mantle and mantle transition zone beneath the ORZ using broad-band seismic data recorded in the vicinity of the rift.

2 DATA AND METHODS

In the summer of 2012, a total of 17 broad-band seismic stations were deployed in northern and central Botswana along a NW–SE profile with a total length of 756 km (Fig. 1), as part of the Seismic Arrays for African Rift Initiation (SAFARI) project (Gao *et al.* 2013; Yu *et al.* 2013). The 17 SAFARI broad-band stations, which were equipped with Quanterra Q330 digitizers and Guralp CMG-3T 120 s sensors, recorded continuously with a sampling rate of 50 Hz until the summer of 2014. Additionally, data from 5 broad-band seismic stations from the 1997–1999 Southern African Seismic Experiment (SASE; Gao *et al.* 2002) are used to enhance coverage and resolution of our data set (Fig. 1).

Data from events in the epicentral distance range of 30–100° are selected with a cut-off magnitude of Mc as defined by $Mc = 5.2 + (\Delta - 30.0)/(180.0 - 30.0) - D/700.0$, where Δ is the epicentral distance in degree and D is the focal depth in km (Liu & Gao 2010). Such an empirical formula was designed to balance the quantity and quality of the data to be processed.

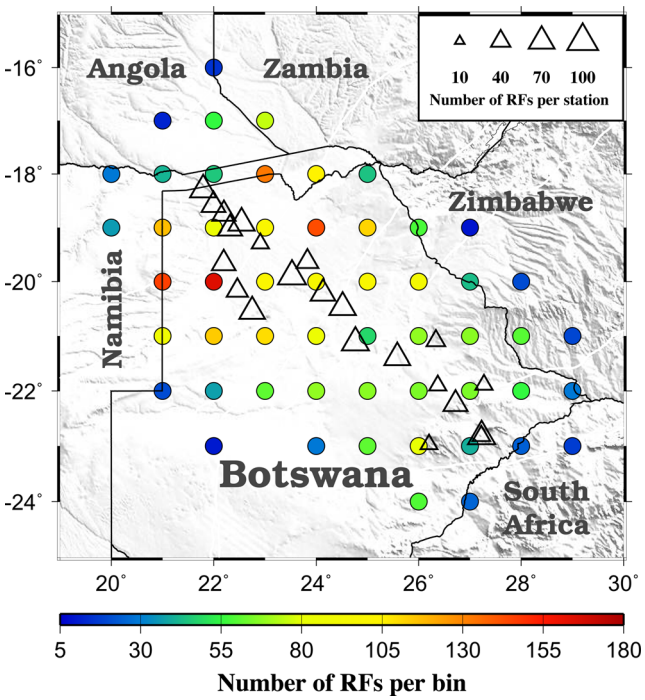

Figure 2. Number of RFs in radius = 1° bins and seismic stations (triangles) used in the study. The size of the triangles is proportional to the number of RFs recorded by the corresponding stations, and the colour of the circles represents the number of RFs per bin.

2.1 Receiver function stacking

The original seismograms are windowed 20 s before and 260 s after the first *P* arrival and are bandpass filtered with a four-pole, two-pass filter in the frequency range of 0.02–0.2 Hz. The filtered three-component seismograms with signal-to-noise ratios (SNR) exceeding 4 on the vertical component are converted into radial RFs by deconvolving the vertical from the radial components using the procedure of Ammon (1991). Before the computation of the RFs, a set of exponential functions with a half width of 30 s and centred at the *PP*-phase are adopted to minimize the degenerating effects of the *PP* arrivals on the RFs (Gao & Liu 2014b). The resulting RFs are subsequently subjected to an SNR-based procedure to select the high-quality RFs (see Gao & Liu 2014a for more information about the specific definition of the SNR and details of the procedure). A total of 1064 high-quality RFs from 22 seismic stations and 159 teleseismic events are obtained (Fig. 1).

We next employ the technique developed by Gao & Liu (2014b) to conduct moveout correction and stacking of *P*-to-*S* converted phases generated from the MTZ discontinuities. The procedure is similar to the common-conversion-point (CCP) method (Dueker & Sheehan 1997) but was developed under the non-plane wavefront assumption, in which the ray-parameters for the direct *P* wave and the converted *S* wave are different, leading to more accurate discontinuity depths and more sharply focused arrivals relative to techniques based on the plane-wave assumption. The geographic coordinates of the ray-piercing points for each of the selected RFs are computed at approximately the middle of the MTZ (535 km) using the IASP91 Earth model. Based on the locations of the ray-piercing points (Fig. 1), we group the RFs into bins with a radius of 1° (Fig. 2). The bins are aligned along the latitudinal and longitudinal lines with a separation of one geographic degree between

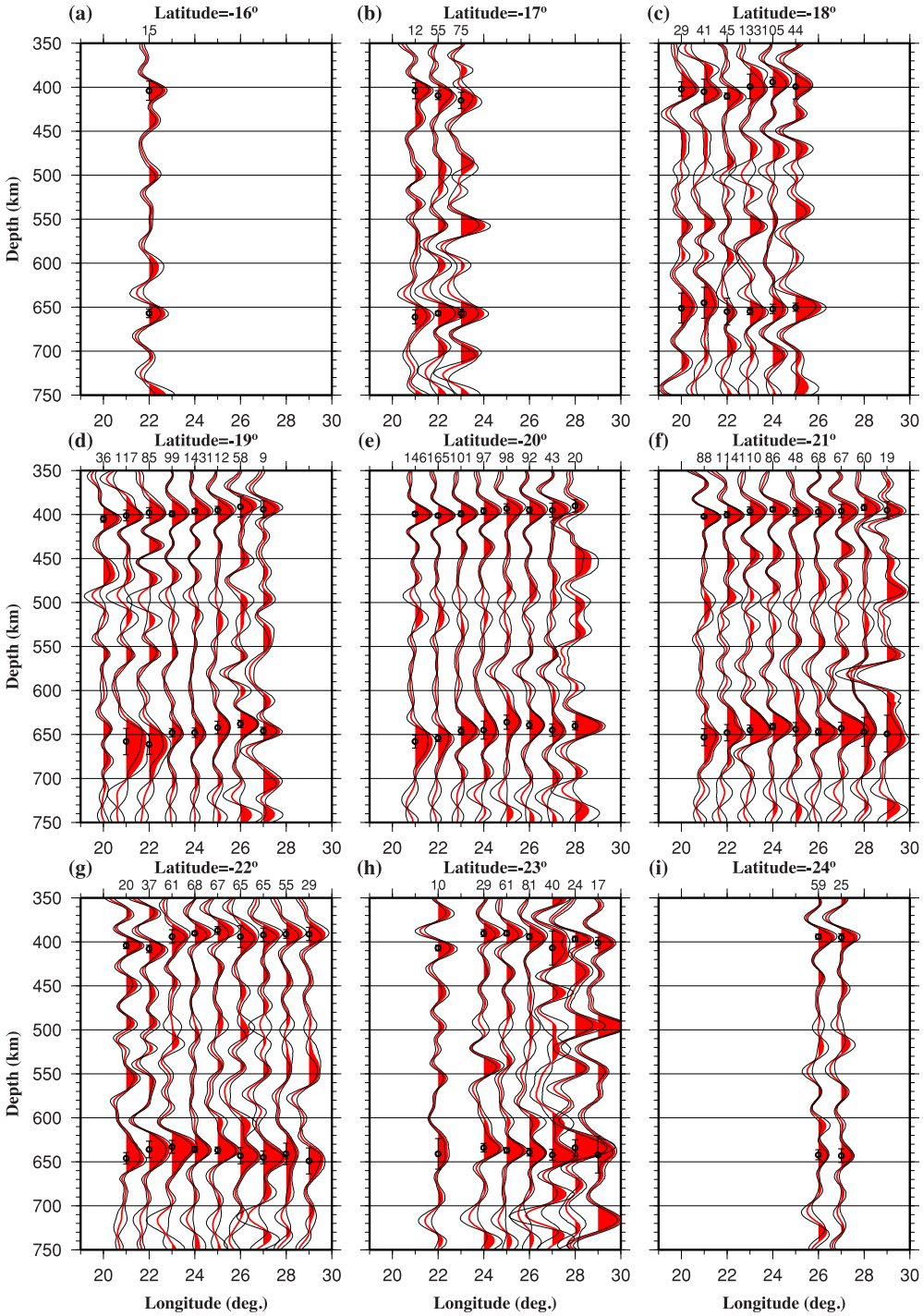

Figure 3. Depth series from stacking of RFs in radius = 1° bins along nine latitudinal profiles. The thick red lines show the mean depth series averaged over all the 50 bootstrap iterations, and the bordering thin black lines show the mean ± two standard deviations. The circles indicate the average depths of the d410 and d660, and the error bars show two standard deviations of the depths. The number on the top of each trace represents the number of RFs in the bin.

adjacent bins. The RFs in a given bin are then moveout corrected and stacked for the depth range of 350–700 km with a vertical resolution of 1 km (eq. 2 in Gao & Liu 2014b). Because a 1-D Earth model is used for the migration and stacking of the RFs, the observed MTZ discontinuity depths are apparent rather than true depths. A bootstrap resampling approach with 50 resampling iterations (Efron & Tibshirani 1986) is applied to obtain the mean and standard deviation (SD) of the MTZ discontinuity depths (Liu *et al.* 2003).

Figs 3 and 4 show all of the resulting depth series along latitudinal and longitudinal profiles, respectively. We also stack the RFs using data recorded by each of the stations (Fig. 5) for the purpose of investigating data quality variations between the stations. Note that the existence of lateral variations in the velocity structure can reduce the stacking amplitude and broaden the peak at the estimated MTZ discontinuity depths. In addition, the stacking results near the edges of the study area are not as reliable as those in the interior due to the lower number of RFs.

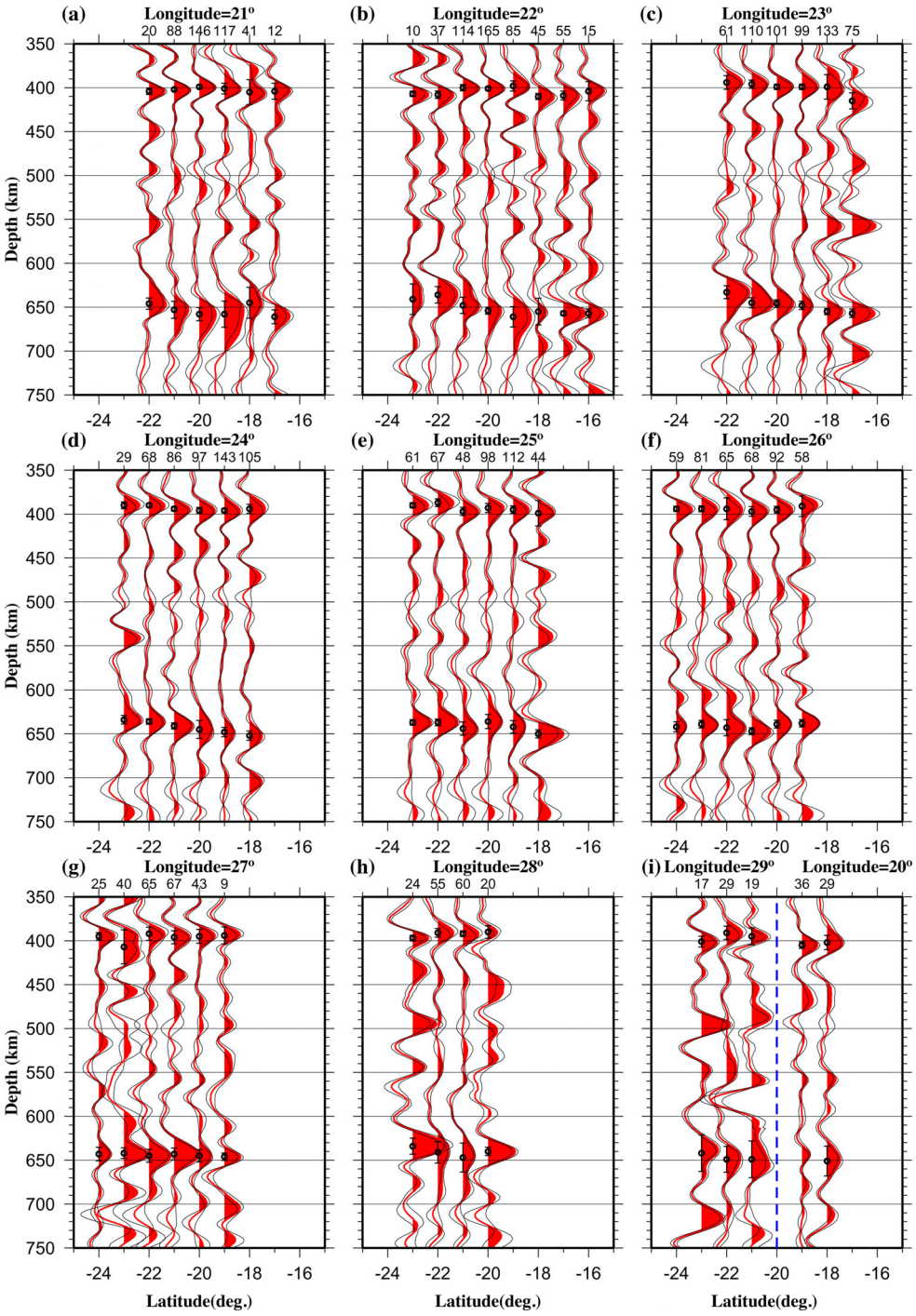

Figure 4. Same as Fig. 3, but for 10 longitudinal profiles. Note plot (i) contains two profiles.

2.2 Traveltime residuals

Both thermal anomalies in the vicinity of and velocity undulations above the MTZ discontinuities can lead to observed variations in the depths of the discontinuities. In order to provide constraints on the interpretation of the resulting MTZ discontinuity depths, we also measure *P*- and *S*-wave traveltime residuals. *P*- and *S*-wave arrivals relative to the IASP91 Earth model are manually picked on the vertical and transverse components, respectively. The accuracy of the hand-picked residuals is dependent on the signal strength relative to the background noise, as well as the sharpness of arrivals. For most of the seismograms, the uncertainty is estimated to be about ± 0.1 s, that is, within five data points from the true value. The mean residual from the event is removed to obtain relative traveltime residuals. The use of relative traveltime residuals minimizes the effects of errors of hypocentral parameters and lateral velocity heterogeneities outside the study area. Events recorded by less than five stations are not used.

We use the following equation to correct for traveltimes due to variations in station elevation (Nolet 2008)

$$\delta t_{ij}^{c} = \delta t_{ij} - \frac{h_i}{v \times \cos[a \sin(R_{ij} \times v)]}, \quad (1)$$

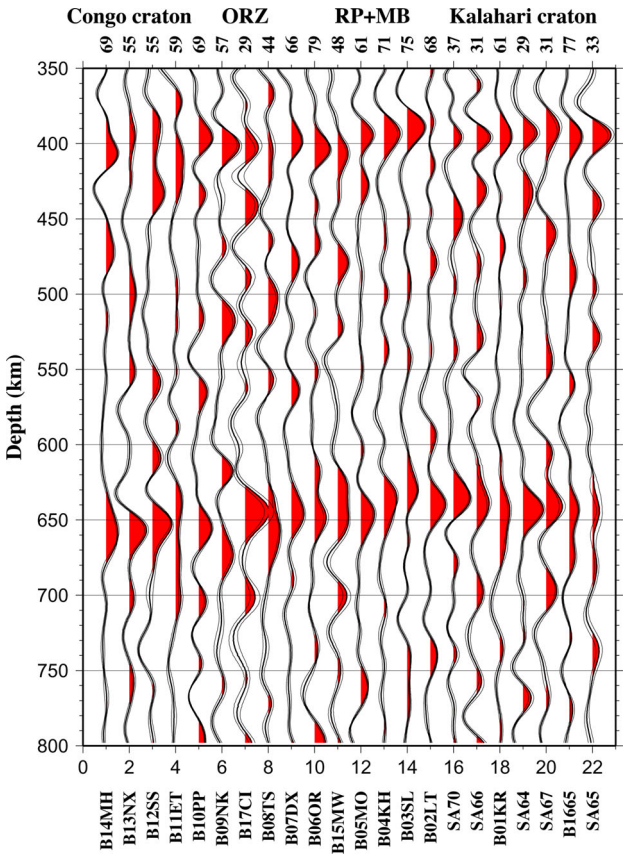

Figure 5. Depth series for each of the stations from moveout correction and stacking of the RFs. The number above each trace is the number of RFs from the station, and the tectonic region that the stations belong to is labelled on the top of the plot. The bottom row shows station names. RP: Rehoboth Province; MB: Magondi Belt.

where h_i is the elevation (in km) for the ith station, δt_{ij} is the original residual (in seconds) observed at the ith station from the jth event, R_{ij} is the ray parameter (in s km^{-1}), and v is the average velocity (in km s^{-1}) in the layer above sea-level. In this study we use 5.5 km s^{-1} for P-wave, and $5.5/\sqrt{3}$ km s^{-1} for S-wave velocities.

3 RESULTS

3.1 Apparent discontinuity depths and MTZ thickness

A total of 53 bins with clearly observable d410 or d660 arrivals are obtained from our data set. Among these bins, 53 of them possess a strong arrival in the depth range of 350–450 km, and 52 have a strong arrival in the depth range of 600–700 km. The arrival with the maximum amplitude in the above ranges is considered as the P-to-S phase from d410 and d660, respectively (Figs 3 and 4). All of the 53 depth series plotted along nine latitudinal lines (from 16°S to 24°S with an increment of 1°) are shown in Fig. 3, and those along 10 longitudinal lines are plotted in Fig. 4. The observed discontinuity depths and the MTZ thickness for each of the bins are summarized in Table 1. To the first-order, the station-specific results (Fig. 5) are similar to those obtained from the 1° bins (Figs 3 and 4). However, due to off-profile variations in the discontinuity depths and the fact that the RFs recorded by a station sample an area that is mostly larger than the 1° size of the bins especially at the d660 depth, the overall strength (relative to noise) and spatial coherency of the d410 and d660 arrivals are higher on the bin-specific depth series (Figs 3 and 4) than on the station-specific ones (Fig. 5). To produce spatially continuous images for the observed depths and MTZ thickness at the bins, we fit the observations using a continuous curvature surface gridding algorithm, with a tension factor of 0.5 (Smith & Wessel 1990; Fig. 6). For the majority of the study area, the SD of the resulting MTZ thickness is less than 5 km (Fig. 6d).

The mean apparent depth of d410 for the entire study area is 398 ± 6 km, that of d660 is 646 ± 7 km and the average MTZ thickness is 248 ± 6 km which is almost identical to the normal thickness of 250 km in the IASP91 Earth model and is statistically consistent with the global average from previous studies (Lawrence & Shearer 2006; Tauzin *et al.* 2008). The apparent depths of both d410 and d660 decrease systematically towards the southeast, from approximately 410 km and 660 km beneath the NW end to 395 km and 645 km near the SE extreme of the study area (Figs 6a and b). The depths beneath the former area (Congo Craton) are identical to those in the IASP91 Earth model, and those beneath the latter (Kalahari Craton in southern Botswana) are about 15 km shallower, an observation that is consistent with the study of Gao *et al.* (2002) for southern Botswana.

The results show that, relative to the immediate adjacent areas, the ORZ displays no observable anomalies in either the apparent depths of the discontinuities or the resulting MTZ thickness. An area of anomalously thin MTZ is observed on the SW corner of the study area, approximately centred at (22°E, 22°S). The anomaly is caused by both a depressed d410 and an uplifted d660, relative to the immediate surrounding areas (Figs 3g and 4b).

3.2 Body-wave traveltime residuals

We have hand-picked 1832 P- and 1356 S-wave residuals from 172 teleseismic events. The residuals are displayed using different approaches. In Figs 7(a) and (b), station averages with standard deviations are displayed along a profile orthogonal to the strike of the ORZ. Such an approach implies that the anomalies in the residuals originate near the surface, which is unlikely. To more reasonably represent the observations, the residuals from individual station-event pairs are displayed at the ray-piercing point at the depth of 100 km, which is approximately the centre of the lithosphere in the study area (Muller *et al.* 2009). The residuals are then projected to an NW–SE oriented profile (Figs 7a and b) and are also plotted as images (Figs 7c and d).

Both the P- and S-wave traveltime residuals decrease towards the SE. The spatially averaged residuals have a peak-to-peak magnitude of about 0.6 s for P and 1.8 s for S waves (Fig. 7). The SE boundary of the ORZ marks the NW end of a linear increase of the traveltime residuals (especially for S waves). Nevertheless, significant traveltime delays are not observed in the ORZ, which is in sharp contrast with other continental rift zones. For instance, across the Baikal rift zone, which was similarly developed along the edge of a stable craton (the Siberian Craton), a P-wave traveltime delay as large as 1 s relative to surrounding areas was observed (Gao *et al.* 2003).

4 DISCUSSION

4.1 Causes of apparent variations in MTZ discontinuity depth

To the first-order, the apparent depths of d410 and d660 (Fig. 6) as well as the P- and S-wave traveltime residuals (Fig. 7) decrease

Table 1. Results of receiver function stacking for each of the bins. clon and clat: longitude and latitude of the bin's center; d410: depth of the d410; sig4: standard deviation of the depth of the d410; d660: depth of the d660; sig6: standard deviation of the depth of the d660; MTZ: mantle transition zone thickness; sigm: standard deviation of MTZ thickness; a4: stacking amplitude of the d410; a6: stacking amplitude of the d660; NRFs: number of receiver functions in the bin.

clon (deg.)	clat (deg.)	d410 (km)	sig4 (km)	d660 (km)	sig6 (km)	MTZ (km)	sigm (km)	a4	a6	NRFs
20.0	−18.0	402	4.1	651	8.5	248	8.2	0.0215	0.0151	29
20.0	−19.0	405	1.8	–	–	–	–	0.0313	0.0000	36
21.0	−17.0	404	4.6	661	4.0	256	5.9	0.0336	0.0268	12
21.0	−18.0	405	7.1	645	8.8	239	11.1	0.0200	0.0150	41
21.0	−19.0	401	3.1	658	7.5	257	8.4	0.0176	0.0189	117
21.0	−20.0	399	0.9	658	3.8	258	3.6	0.0218	0.0265	146
21.0	−21.0	402	0.8	653	4.8	250	4.7	0.0208	0.0197	88
21.0	−22.0	404	1.9	646	3.3	242	3.7	0.0269	0.0309	20
22.0	−16.0	404	5.5	657	2.5	253	5.1	0.0292	0.0280	15
22.0	−17.0	409	2.6	657	1.3	247	2.8	0.0175	0.0259	55
22.0	−18.0	410	1.7	655	7.6	244	7.8	0.0207	0.0093	45
22.0	−19.0	398	2.9	661	5.8	263	6.1	0.0171	0.0218	85
22.0	−20.0	401	0.9	654	2.0	253	2.1	0.0245	0.0212	165
22.0	−21.0	400	1.8	648	4.6	247	5.1	0.0167	0.0172	114
22.0	−22.0	408	2.1	636	4.7	227	5.4	0.0277	0.0356	37
22.0	−23.0	407	1.5	641	8.7	233	8.8	0.0464	0.0264	10
23.0	−17.0	415	4.6	657	2.4	241	4.5	0.0148	0.0198	75
23.0	−18.0	399	7.0	655	1.8	255	7.0	0.0132	0.0147	133
23.0	−19.0	399	1.5	648	2.4	249	2.9	0.0264	0.0170	99
23.0	−20.0	399	1.5	646	2.2	246	2.7	0.0222	0.0243	101
23.0	−21.0	396	2.4	645	2.9	249	4.0	0.0189	0.0244	110
23.0	−22.0	394	3.9	633	3.7	239	4.7	0.0165	0.0241	61
24.0	−18.0	394	2.6	652	2.7	258	4.4	0.0258	0.0213	105
24.0	−19.0	396	1.3	648	2.7	251	2.7	0.0319	0.0183	143
24.0	−20.0	396	1.8	645	5.1	249	5.1	0.0266	0.0179	97
24.0	−21.0	394	1.3	641	1.8	246	1.8	0.0215	0.0267	86
24.0	−22.0	390	1.1	636	1.6	245	2.1	0.0289	0.0251	68
24.0	−23.0	390	2.0	634	2.4	244	3.2	0.0266	0.0298	29
25.0	−18.0	399	7.2	650	2.3	250	7.7	0.0207	0.0329	44
25.0	−19.0	395	2.1	642	3.6	246	4.0	0.0237	0.0173	112
25.0	−20.0	393	2.6	636	4.0	242	4.8	0.0227	0.0173	98
25.0	−21.0	397	2.3	644	3.8	246	4.1	0.0246	0.0194	48
25.0	−22.0	387	2.2	637	1.9	249	2.6	0.0193	0.0254	67
25.0	−23.0	390	1.5	637	1.6	247	1.9	0.0246	0.0285	61
26.0	−19.0	391	5.9	638	2.1	247	6.4	0.0172	0.0207	58
26.0	−20.0	395	1.9	639	2.2	243	2.4	0.0195	0.0214	92
26.0	−21.0	397	2.8	647	2.0	250	3.1	0.0222	0.0247	68
26.0	−22.0	394	6.2	643	4.6	249	8.2	0.0171	0.0188	65
26.0	−23.0	394	1.7	639	2.2	245	2.6	0.0205	0.0196	81
26.0	−24.0	394	1.5	642	2.8	247	3.0	0.0250	0.0166	59
27.0	−19.0	394	4.9	646	2.1	252	5.4	0.0299	0.0307	9
27.0	−20.0	395	4.0	645	3.5	250	5.4	0.0239	0.0213	43
27.0	−21.0	396	3.7	643	3.5	246	4.4	0.0155	0.0257	67
27.0	−22.0	392	3.8	645	3.7	252	6.0	0.0159	0.0210	65
27.0	−23.0	407	9.7	642	3.1	235	10.3	0.0114	0.0185	40
27.0	−24.0	395	2.2	643	3.9	248	5.1	0.0309	0.0244	25
28.0	−20.0	390	3.6	640	2.4	250	3.6	0.0128	0.0270	20
28.0	−21.0	392	1.6	647	8.2	255	8.3	0.0249	0.0181	60
28.0	−22.0	391	2.5	641	6.1	250	6.3	0.0226	0.0173	55
28.0	−23.0	397	1.6	634	4.6	237	4.4	0.0133	0.0303	24
29.0	−21.0	395	4.8	649	10.5	253	12.5	0.0183	0.0192	19
29.0	−22.0	391	3.8	649	7.4	258	9.1	0.0254	0.0190	29
29.0	−23.0	401	3.1	642	10.4	241	11.0	0.0222	0.0172	17

from the Congo Craton at the NW part of the profile towards the Kalahari Craton at the SE. The fact that the MTZ thickness remains the same throughout most of the study area suggests that the apparent variations of the observed depths are mainly caused by lateral velocity variations in the upper mantle, probably by variations in the thickness of the lithosphere. In the following, we quantify this using our RF results and lithospheric thickness estimated from previous studies (James *et al.* 2001; Muller *et al.* 2009).

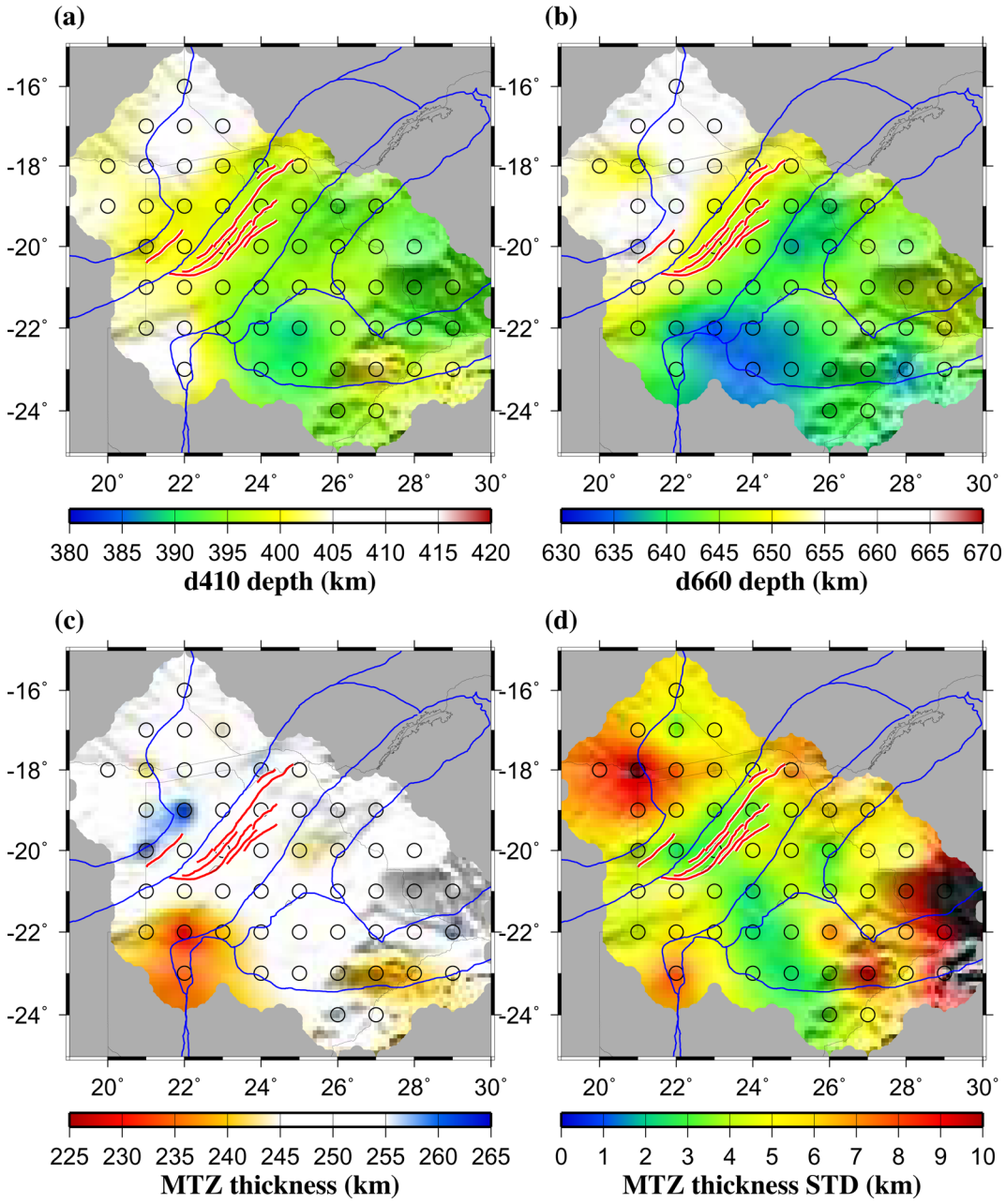

Figure 6. (a) Smoothed spatial distribution of resulting d410 depth; (b) same as (a) but for d660; (c) MTZ thickness; (d) standard deviations of the MTZ thickness measurements. Circles indicate the centre of circular areas with high-quality measurements. Note that in (a)–(c), only measurements that are 5 or more km different from the corresponding global average are coloured.

As discussed above, relative to the Congo Craton, both d410 and d660 beneath the Kalahari Craton are uplifted by about 15 km. Under the assumption that this apparent uplift is purely caused by velocity anomalies, we estimate that a 15 km uplift corresponds to a Vp anomaly of +1.2 per cent in the depth range of 0–410 km using the approach of Gao & Liu (2014b). If the anomalous zone is limited to a 100 km thick layer, the required anomaly is about 5 per cent, and this value reduces to about 3 per cent if the thickness is 150 km. In addition, the velocity anomalies resulting in a 15 km apparent uplift of both d410 and d660 can produce a *P*-wave traveltime residual of about −0.6 s, which is almost exactly what was observed (Fig. 7). To estimate the predicted *S*-wave traveltime residual using the apparent depression of the discontinuities, the γ value, which is the ratio between *S*- and *P*-wave relative velocity anomalies, that is, $\gamma = d\ln(V_s)/d\ln(V_p)$, is required. Under the assumption of $\gamma = 1.7$, which is the same as that found for the stable central and eastern United States (Gao & Liu 2014a), the *S*-wave velocity anomaly is about +2 per cent and the predicted *S*-wave traveltime residual is −1.8 s, which is once again consistent with the observed value (Fig. 7).

We next explore the possibility that the observed velocity anomalies originate from lateral variations of lithospheric thickness beneath the study area. Seismic tomography studies indicated that the Kalahari Cratonic root extends to at least 250 km and perhaps as deep as 300 km (James *et al.* 2001). On the other hand, Muller *et al.* (2009) found the lithospheric thickness in the vicinity of the Damara belt in the ORZ to be approximately 160 km. These studies suggest that beneath the Kalahari Craton, the lithosphere is

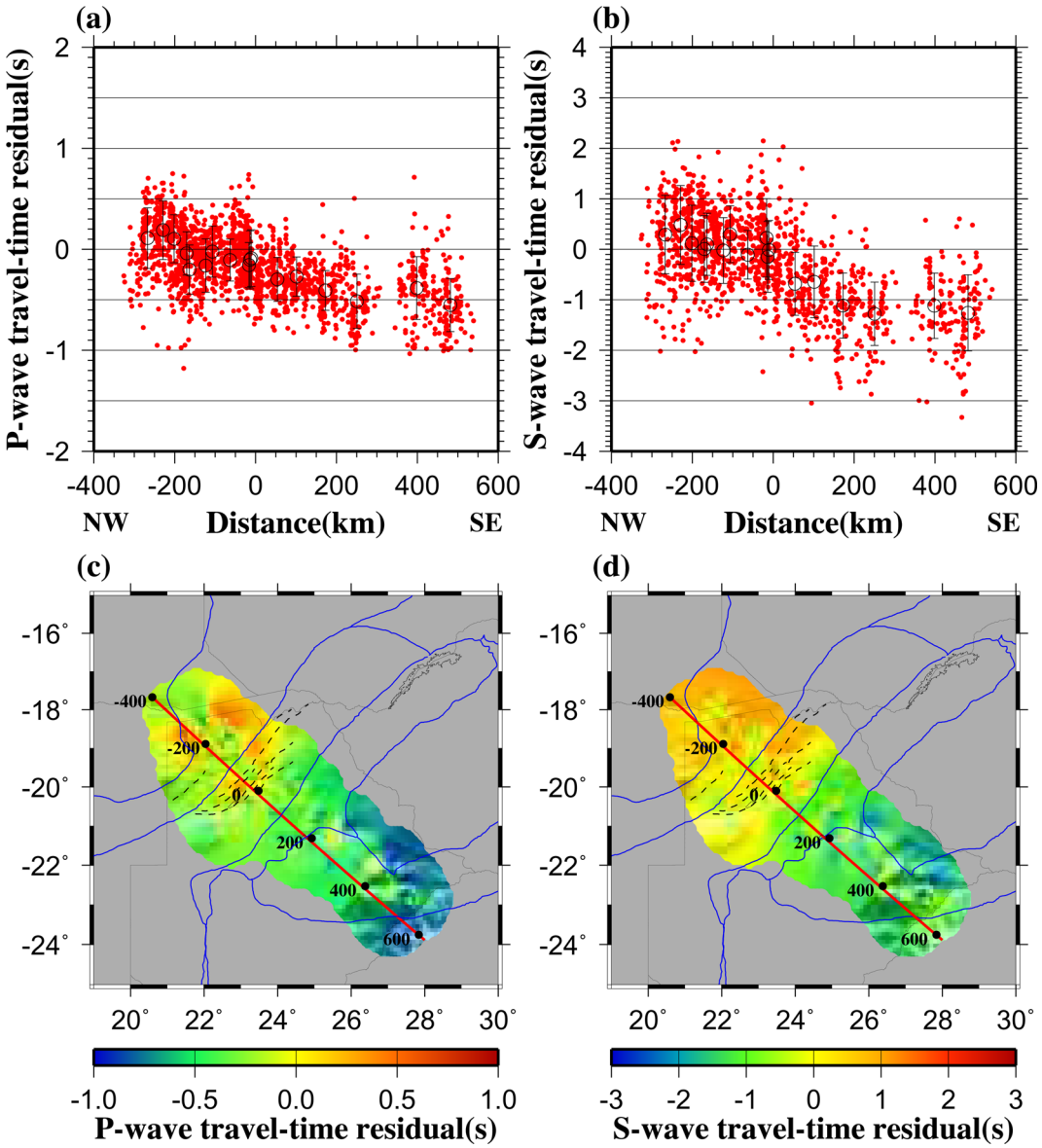

Figure 7. Teleseismic *P*- and *S*-wave traveltime residuals displayed above the ray-piercing points at 100 km depth. (a) *P*-wave residuals projected on to the profile shown in (c). Dots are individual event values, and circles with error bars are station-averaged values. (b) Same as (a) but for *S*-wave residuals. (c) Spatial distribution of *P*-wave residuals. (d) Spatial distribution of *S*-wave residuals. The numbers along the profile in (c) and (d) indicate the distance in km from the SE boundary fault of the ORZ.

approximately 100–150 km thicker than that beneath the northwestern part of the study area. If we assume that this 100–150 km excessive lithospheric thickness is solely responsible for the observed 15 km apparent uplift of the MTZ discontinuities and variations in traveltime residuals, the required *P*-wave velocity contrast is 3–5 per cent between the lithosphere and the asthenosphere. Velocity contrasts of similar magnitude are commonly found in numerous previous seismic tomography and RF studies (e.g. Gao *et al.* 2003; Li *et al.* 2003; Rychert *et al.* 2007; Eaton *et al.* 2009).

The normal apparent discontinuity depths beneath the Congo Craton and the ORZ suggest normal (relative to the IASP91 Earth model) upper mantle *P*- and *S*-wave velocities. This is drastically different from the mature segments of the EARS beneath which greater-than-normal apparent discontinuity depths (e.g. Thompson *et al.* 2015) and lower-than-normal velocities (Bastow 2012) have been reported. Similarly, the shallow d410 and d660 beneath the Kalahari Craton imply higher-than-normal velocities and are consistent with seismic tomographic studies (James *et al.* 2001). We note that considerable discrepancies in the experimentally determined Clapeyron slopes were found among previous studies (see Litasov *et al.* 2005 and Ghosh *et al.* 2013 for some examples), making it difficult to reliably convert undulations in the observed MTZ discontinuity depths into temperature anomalies. Using the Clapeyron slopes of $+2.9$ MPa K^{-1} for d410 and -2.1 MPa K^{-1} for d660 (Bina & Helffrich 1994), the resulting MTZ thickness of 248 ± 6 km corresponds to a thermal anomaly ranging between -34 K and $+68$ K.

The anomalously thin MTZ observed on the SW corner of the study area (Fig. 6c) has an estimated thickness of 235 km, corresponding to an estimated thermal anomaly of $+127$ K. This abnormally thin MTZ, if confirmed, could suggest significant transferring of heat from the lower to the upper mantle beneath western

Botswana. Such a transfer might be related to the African Superplume, which is thought to be confined in the lower mantle beneath southern Africa (James *et al.* 2001; Gao *et al.* 2002). Unfortunately, this area is located on the edge of the region sampled by a limited number of RFs (Figs 1 and 2).

The above discussions assume anhydrous conditions. Some previous MTZ studies involved the presence of water in the MTZ to explain the observed larger-than-normal MTZ thickness (Blum & Shen 2004; Cao & Levander 2010; Mohamed *et al.* 2014; Thomson *et al.* 2015), and one of them (Blum & Shen 2004) investigated the MTZ beneath the Kalahari Craton. Water can uplift the d410 and depress the d660, resulting in a thicker MTZ (Litasov *et al.* 2005). The addition of water also reduces seismic velocities in the MTZ (Inoue *et al.* 1998) and thus leads to an apparent MTZ thickening. Therefore, in order to produce the observed normal apparent MTZ thickness, higher-than-normal temperature in the MTZ is required to reduce the thickness. While it is possible that the effects of water and temperature can cancel each other and result in a normal MTZ thickness, as observed, the chance for this to happen is not high. This is because it requires a specific combination of the amplitude of the temperature anomaly and the amount of water through out most of the study area where normal MTZ thickness is observed. Additionally, some studies suggested that excessive amount of water can increase the pulse width of d410 and decrease its amplitude (Smyth & Frost 2002; Van der Meijde *et al.* 2003). This is contradictory to the sharp arrivals associated with both the d410 and d660 discontinuities (Figs 3 and 4). Therefore, while the pervasive existence of water in the study area cannot be completely ruled out, an anhydrous MTZ with nearly normal temperature can satisfactorily explain the observations.

4.2 Implications for rifting mechanisms

The observed normal MTZ thickness, lack of significant traveltime residuals and the absence of elevated mantle conductivity (Khoza *et al.* 2013) associated with the incipient ORZ suggest the absence of high-temperature anomalies in both the MTZ and the upper mantle, ruling out contributions of one or more mantle plumes in rift initiation and favouring a 'passive' origin.

A recent geodetic study (Malservisi *et al.* 2013) suggested that with respect to the African continent, the rigid South African block rotates clockwise, probably along the Damara belt. Such differential movements between relatively rigid tectonic blocks can rupture the pre-existing weak zones along edges of the blocks. The fractures can then propagate downwards through the lithosphere without mantle upwelling anomalies, and rifting processes can continue as long as the regional dominant stresses are extensional or transtensional. A likely environment for reactivation of shear zones adjacent to the ORZ is the transcontinental Mwembeshi dislocation zone which experiences left-lateral transtension as the consequence of differential extension between Nubia and Somalia (Daly *et al.* 1989). The Mwembeshi shear zone, which intersects the Luangwa and Malawi rift zones farther to the northeast of the ORZ, has been suggested to exert geometrical control on rift basin development within the EARS (Versfelt & Rosendahl 1989). Similar lithospheric-scale Proterozoic suture shear zones have been cited as a possible origin for the Kenya Rift (Birt *et al.* 1997). Differential movements between tectonic blocks in a relatively stable tectonic plate can originate from many factors, such as differences in the direction and/or strength of mantle flow (either as driving or resistant forces), uneven distribution of ridge push and slab pull forces across the plate, spatially varying far-field stress from continental collision, and non-uniform influence of mantle upwelling or downwelling (e.g. Sabadini & Guinchi 1992; Doglioni 1993). We speculate that for the ORZ, variations of lithospheric thickness combined with the presence of previously ruptured lithosphere give rise to one or more of the above heterogeneities, leading to rift initiation. Such a passive rifting model is consistent with conclusions from the study of Leseane *et al.* (2015) that the ORZ could be initiated through fluid-assisted lithospheric weakening without asthenospheric involvement. Passive stretching of the lithosphere may eventually lead to active upwelling of the asthenosphere and resulting in the transition from passive to active rifting (Huismans *et al.* 2001). This model could explain why most of the world's continental rifts developed along the edges of cratonic blocks, where rapid changes of lithospheric thickness are commonly found (Keller *et al.* 1991).

5 CONCLUSIONS

This first receiver function study of the incipient ORZ reveals a normal MTZ thickness, arguing against a strong thermal anomaly in the upper mantle and MTZ beneath most of the study area. The apparently shallower-than-normal MTZ discontinuities observed beneath the Kalahari Craton can be explained by the existence of a lithosphere that is 100–150 km thicker than that beneath the Congo Craton and the Damara belt. In addition, the ORZ is not associated with significant delays in teleseismic *P*- and *S*-wave traveltime residuals, implying the absence of significant mantle anomalies beneath the ORZ. These observations are inconsistent with the existence of mantle plumes or a broadly upwarped asthenosphere beneath the study area. Instead, they provide unprecedented supporting evidence for a model of rift initiation involving lithospheric fracturing due to differential movements between tectonic blocks along pre-existing zones of weakness such as edges of cratonic blocks.

ACKNOWLEDGEMENTS

This study is part of the passive seismic component of an interdisciplinary project funded by the United States National Science Foundation (NSF) Continental Dynamics Program. We appreciate discussions with and encouragements from other participants of the project. Careful reviews by three anonymous reviewers and Editor G.R. Keller significantly improved the manuscript. We thank the Program for Array Seismic Studies of the Continental Lithosphere (PASSCAL) Instrument Center for equipment and logistical support, and the Incorporated Research Institutions for Seismology (IRIS) Data Management Center for achieving both the SAFARI and SASE data sets used in the study. Field assistance provided by Angela M. Reusch from PASSCAL and Keletso Kaisara from the University of Botswana is greatly appreciated. YY was partially supported by the China Scholarship Council under contract No. 2011645027 and CR was partly supported by the Missouri University of Science and Technology Chancellor's Fellowship. The field and data analysis tasks related to this study were supported by NSF grant EAR-1009946 to SG and KL.

REFERENCES

Ammon, C.J., 1991. The isolation of receiver effects from teleseismic *P*-waveforms, *Bull. seism. Soc. Am.,* **81,** 2504–2510.

Bastow, I.D., 2012. Relative arrival-time upper-mantle tomography and the elusive background mean, *Geophys. J. Int.,* **190,** 1271–1278.

Begg, G.C. *et al.*, 2009. The lithospheric architecture of Africa: Seismic tomography, mantle petrology, and tectonic evolution, *Geosphere,* **5,** 23–50.

Bina, C.R. & Helffrich, G., 1994. Phase transition Clapeyron slopes and transition zone seismic discontinuity topography, *J. geophys. Res.,* **99,** 15 853–15 860.

Birt, C.S., Maguire, P.K.H., Khan, M.A., Thybo, H., Keller, G.R. & Patel, J., 1997. The influence of pre-existing structures on the evolution of the southern Kenya Rift Valley-evidence from seismic and gravity studies, *Tectonophysics,* **278,** 211–242.

Blum, J. & Shen, Y., 2004. Thermal, hydrous, and mechanical states of the mantle transition zone beneath southern Africa, *Earth planet. Sci. Lett.,* **217,** 367–378.

Bufford, K.M. *et al.*, 2012. Geometry and faults tectonic activity of the Okavango Rift Zone, Botswana: evidence from magnetotelluric and electrical resistivity tomography imaging, *J. Afr. Earth. Sci.,* **65,** 61–71.

Cao, A. & Levander, A., 2010. High-resolution transition zone structures of the Gorda slab beneath the western United States: implication for deep water subduction, *J. geophys. Res.,* **115,** B07301, doi:10.1029/2009JB006876.

Daly, M.C., Chorowicz, J. & Fairhead, J.D., 1989. Rift basin evolution in Africa: the influence of reactivated steep basement shear zones, in *Inversion Tectonics,* Vol. 44, pp. 309–334, eds. Cooper, M.A. & Williams, G.D., Geol. Soc. Spec. Pub.

Doglioni, C., 1993. Geological evidence for a global tectonic polarity, *J. geol. Soc. Lond.,* **150,** 991–1002.

Dueker, K.G. & Sheehan, A.F., 1997. Mantle discontinuity structure from midpoint stacks of converted P to S waves across the Yellowstone hotspot track, *J. geophys. Res.,* **102,** 8313–8327.

Eaton, D.W., Darbyshire, F.A., Evans, R.L., Grutter, H., Jones, A.G. & Yuan, X., 2009. The elusive lithosphere-asthenosphere boundary (LAB) beneath cratons, *Lithos,* **109,** 1–22.

Ebinger, C.J., Crow, M.J., Rosendahl, B.R., Livingstone, D.A. & LeFournier, J., 1984. Structural evolution of the Malawi rift, Africa, *Nature,* **308,** 627–629.

Efron, B. & Tibshirani, R., 1986. Bootstrap methods for standard errors, confidence intervals, and other measures of statistical accuracy, *Stat. Sci.,* **1,** 54–75.

Gao, S.S. & Liu, K.H., 2014a. Mantle transition zone discontinuities beneath the contiguous United States, *J. geophys. Res.,* **119,** 6452–6468.

Gao, S.S. & Liu, K.H., 2014b. Imaging mantle discontinuities using multiply-reflected *P*-to-*S* conversions, *Earth planet. Sci. Lett.,* **402,** 99–106.

Gao, S.S., Silver, P.G. & Liu, K.H., 2002. Mantle discontinuities beneath southern Africa, *Geophys. Res. Lett.,* **29,** 1291–1294.

Gao, S.S., Liu, K.H., Davis, P.M., Slack, P.D., Zorin, Y.A., Mordvinova, V.V. & Kozhevnikov, V.M., 2003. Evidence for small-scale mantle convection in the upper mantle beneath the Baikal rift zone, *J. geophys. Res.,* **108**(B4), 2194, doi:10.1029/2002JB002039.

Gao, S.S. *et al.*, 2013. Seismic Arrays to Study African Rift Initiation, *EOS, Trans. Am. geophys. Un.,* **94,** 213–214.

Ghosh, S., Ohtani, E., Litasov, K.D., Suzuki, A., Dobson, D. & Funakoshi, K., 2013. Effect of water in depleted mantle on post-spinel transition and implication for 660 km seismic discontinuity, *Earth planet. Sci. Lett.,* **371–372,** 103–111.

Hanson, R.E., 2003. Proterozoic geochronology and tectonic evolution of southern Africa, *Geol. Soc. Spec. Pub.,* **206,** 427–463.

Helffrich, G., 2000. Topography of the transition zone seismic discontinuities, *Rev. Geophys.,* **38,** 141–158.

Huerta, A.D., Nyblade, A.A. & Reusch, A.M., 2009. Mantle transition zone structure beneath Kenya and Tanzania: more evidence for a deep-seated thermal upwelling in the mantle, *Geophys. J. Int.,* **177,** 1249–1255.

Huismans, R.S., Podladchikov, Y.Y. & Cloetingh, S., 2001. Transition from passive to active rifting: relative importance of asthenospheric doming and passive extension of the lithosphere, *J. geophys. Res.,* **106,** 11 271–11 291.

Inoue, T., Weidner, D.J., Northrup, P.A. & Parise, J.B., 1998. Elastic properties of hydrous ringwoodite (Q-phase) in Mg_2SiO_4, *Earth planet. Sci. Lett.,* **160,** 107–113.

James, D.E., Fouch, M.J., VanDecar, J.C. & Van Der Lee, S., 2001. Tectospheric structure beneath southern Africa, *Geophys. Res. Lett.,* **28,** 2485–2488.

Keller, G.R., Khan, M.A., Morgan, P., Wendlandt, R.F., Baldridge, W.S., Olsen, K.H., Prodehl, C. & Braile, L.W., 1991. A comparative study of the Rio Grande and Kenya rifts, *Tectonophysics,* **197,** 355–371.

Khoza, T.D., Jones, A.G., Muller, M.R., Evans, R.L., Miensopust, M.P. & Webb, S.J., 2013. Lithospheric structure of an Archean craton and adjacent mobile belt revealed from 2-D and 3-D inversion of magnetotelluric data: example from southern Congo craton in northern Namibia, *J. geophys. Res.,* **118,** 4378–4397.

Kinabo, B.D., Hogan, J.P., Atekwana, E.A., Abdelsalam, M.G. & Modisi, M.P., 2008. Fault growth and propagation during incipient continental rifting: insights from a combined aeromagnetic and Shuttle Radar Topography Mission digital elevation model investigation of the Okavango Rift Zone, northwest Botswana, *Tectonics,* **27,** TC3013, doi:10.1029/2007TC002154.

Lawrence, J.F. & Shearer, P.M., 2006. A global study of transition zone thickness using receiver functions, *J. geophys. Res.,* **111,** B06307, doi:10.1029/2005JB003973.

Leseane, K., Atekwana, E.A., Mickus, K.L., Abdelsalam, M.G., Shemang, E.M. & Atekwana, E.A., 2015. Thermal perturbations beneath the incipient Okavango Rift Zone, northwest Botswana, *J. geophys. Res.,* **120,** 1210–1228.

Li, A., Forsyth, D.W. & Fischer, K.M., 2003. Shear velocity structure and azimuthal anisotropy beneath eastern North America from Rayleigh wave inversion, *J. geophys. Res.,* **108,** doi:10.1029/2002JB02259.

Litasov, K.D., Ohtani, E., Suzuki, A. & Funakoshi, K., 2005. Wet subduction versus cold subduction, *Geophys. Res. Lett.,* **32,** L13312, doi:10.1029/2005GL022921.

Liu, K.H. & Gao, S.S., 2006. Mantle transition zone discontinuities beneath the Baikal rift and adjacent areas, *J. geophys. Res.,* **111,** B11301, doi:10.1029/2005JB004099.

Liu, K.H. & Gao, S.S., 2010. Spatial variations of crustal characteristics beneath the Hoggar swell, Algeria revealed by systematic analyses of receiver functions from a single seismic station, *Geochem. Geophys. Geosys.,* **11,** Q08011, doi:10.1029/2010GC003091.

Liu, K.H., Gao, S.S., Silver, P.G. & Zhang, Y., 2003. Mantle layering across central South America, *J. geophys. Res.,* **108,** 2510, doi:10.1029/2002JB002208.

Malservisi, R., Hugentobler, U., Wonnacott, R. & Hackl, M., 2013. How rigid is a rigid plate? Geodetic constraint from the TrigNet CGPS network, South Africa, *Geophys. J. Int.,* **192,** 918–928.

McCourt, S., Armstrong, R.A., Jelsma, H. & Mapeo, R.B.M., 2013. New U-Pb SHRIMP ages from the Lubango region, SW Angola: insights into the Palaeoproterozoic evolution of the Angolan Shield, southern Congo Craton, Africa, *J. geol. Soc. Lond,* **170,** 353–363.

Miensopust, M.P., Jones, A.G., Muller, M.R., Garcia, X. & Evans, R.L., 2011. Lithospheric structures and precambrian terrane boundaries in northeastern Botswana revealed through magnetotelluric profiling as part of the southern African magnetotelluric experiment, *J. geophys. Res.,* **116,** B02401, doi:10.1029/2010JB007740.

Modisi, M.P., Atekwana, E.A., Kampunzu, A.B. & Ngwisanyi, T.H., 2000. Rift kinematics during the incipient stages of continental extension: evidence from the nascent Okavango rift basin, northwest Botswana, *Geology,* **28,** 939–942.

Mohamed, A.A., Gao, S.S., Elsheikh, A.A., Liu, K.H., Yu, Y. & Fat-Helbary, R.E., 2014. Seismic imaging of mantle transition zone discontinuities beneath the northern Red Sea and adjacent areas, *Geophys. J. Int.,* **199,** 648–657.

Mulibo, G.D. & Nyblade, A.A., 2013. Mantle transition zone thinning beneath eastern Africa: evidence for a whole-mantle superplume structure, *Geophys. Res. Lett.,* **40,** 3562–3566.

Muller, M.R. *et al.*, 2009. Lithospheric structure, evolution and diamond prospectivity of the Rehoboth Terrane and Western Kaapvaal Craton, Southern Africa: constraints from broadband magnetotellurics, *Lithos,* **112,** 93–105.

Nolet, G., 2008. *A Breviary of Seismic Tomography,* Cambridge Univ. Press.

Nyblade, A.A., Owens, T.J., Gurrola, H., Ritsema, J. & Langston, C.A., 2000. Seismic evidence for a deep upper mantle thermal anomaly beneath east Africa, *Geology,* **28,** 599–602.

Owens, T.J., Nyblade, A.A., Gurrola, H. & Langston, C.A., 2000. Mantle transition zone structure beneath Tanzania, East Africa, *Geophys. Res. Lett.,* **27,** 827–830.

Reeves, C.V., 1972. Rifting in the Kalahari? *Nature,* **237,** 95–96.

Ringwood, A.E., 1975. *Composition and Petrology of the Earth's Mantle,* McGraw-Hill.

Rychert, C.A., Rondenay, S. & Fischer, K.M., 2007. *P*-to-*S* and *S*-to-*P* imaging of a sharp lithosphere-asthenosphere boundary beneath eastern North America, *J. geophys. Res.,* **112,** B08314, doi:10.1029/2006JB004619.

Sabadini, R. & Giunchi, G., 1992. Plate motion and dragging of the upper mantle: lateral variations of lithospheric thickness and their implications for intraplate deformation, *Geophys. Res. Lett.,* **19,** 749–752.

Schmeling, H., 2010. Dynamic models of continental rifting with melt generation, *Tectonophysics,* **480,** 33–47.

Sengor, A.M. & Burke, K., 1978. Relative timing of rifting and volcanism on Earth and its tectonic implications, *Geophys. Res. Lett.,* **5,** 419–421.

Smith, W.H.F. & Wessel, P., 1990. Gridding with continuous curvature splines in tension, *Geophysics,* **55,** 293–305.

Smyth, J.R. & Frost, D.J., 2002. The effect of water on the 410-km discontinuity: an experimental study, *Geophys. Res. Lett.,* **29,** 1–4.

Stern, R.J., 1994. Arc-assembly and continental collision in the Neoproterozoic African orogen: implications for the consolidation of Gondwanaland, *Annu. Rev. Earth planet. Sci.,* **22,** 319–351.

Tauzin, B., Debayle, E. & Wittlinger, G., 2008. The mantle transition zone as seen by global *Pds* phases: no clear evidence for a thin transition zone beneath hotspots, *J. geophys. Res.,* **113,** B08309, doi:10.1029/2007JB005364.

Thompson, D.A., Hammond, J.O.S., Kendall, J.-M., Stuart, G.W., Helffrich, G., Keir, D., Ayele, A. & Goitom, B., 2015. Hydrous upwelling across the mantle transition zone beneath the Afar Triple Junction, *Geochem. Geophys. Geosyst.,* **16,** 834–846.

van der Meijde, M., Marone, F., Giardini, D. & van der Lee, V., 2003. Seismic evidence for water deep in Earth's upper mantle, *Science,* **300,** 1556–1558.

Versfelt, J. & Rosendahl, B.R., 1989. Relationships between pre-rift structure and rift architecture in Lakes Tanganyika and Malawi, East Africa, *Nature,* **337,** 354–357.

White, R. & McKenzie, D., 1989. Magmatism at rift zones: the generation of volcanic continental margins and flood basalts, *J. geophys. Res.,* **94,** 7685–7729.

Wilson, D., Aster, R., Ni, J., Grand, S., West, M., Gao, W., Baldridge, W.S. & Semken, S., 2005. Imaging the seismic structure of the crust and upper mantle beneath the Great Plains, Rio Grande Rift, and Colorado Plateau using receiver functions, *J. geophys. Res.,* **110,** B05306, doi:10.1029/2004JB003492.

Yu, Y. *et al.*, 2013. Crustal and mantle structure and anisotropy beneath the incipient segments of the East African Rift System: preliminary results from the ongoing SAFARI, *AGU Fall Meet. Abstracts,* **1,** 2542.